

# Experimental and Theoretical Investigations of Energy Transfer and Hydrogen-Bond Breaking in the Water Dimer

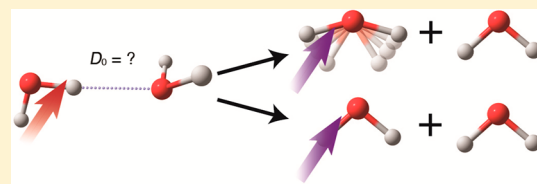
Lee C. Ch'ng,<sup>†</sup> Amit K. Samanta,<sup>†</sup> Gábor Czakó,<sup>‡,§</sup> Joel M. Bowman,<sup>\*,‡</sup> and Hanna Reisler<sup>\*,†</sup>

<sup>†</sup>Department of Chemistry, University of Southern California, Los Angeles, California 90089-0482, United States

<sup>‡</sup>Department of Chemistry and Cherry L. Emerson Center for Scientific Computation, Emory University, Atlanta, Georgia 30322, United States

Web-Enhanced Feature Supporting Information

**ABSTRACT:** The hydrogen bonding in water is dominated by pairwise dimer interactions, and the predissociation of the water dimer following vibrational excitation is reported here. Velocity map imaging was used for an experimental determination of the dissociation energy ( $D_0$ ) of  $(D_2O)_2$ . The value obtained,  $1244 \pm 10 \text{ cm}^{-1}$  ( $14.88 \pm 0.12 \text{ kJ/mol}$ ), is in excellent agreement with the calculated value of  $1244 \pm 5 \text{ cm}^{-1}$  ( $14.88 \pm 0.06 \text{ kJ/mol}$ ). This agreement between theory and experiment is as good as the one obtained recently for  $(H_2O)_2$ . In addition, pair-correlated water fragment rovibrational state distributions following vibrational predissociation of  $(H_2O)_2$  and  $(D_2O)_2$  were obtained upon excitation of the hydrogen-bonded OH and OD stretch fundamentals, respectively. Quasi-classical trajectory calculations, using an accurate full-dimensional potential energy surface, are in accord with and help to elucidate experiment. Experiment and theory find predominant excitation of the fragment bending mode upon hydrogen bond breaking. A minor channel is also observed in which both fragments are in the ground vibrational state and are highly rotationally excited. The theoretical calculations reveal equal probability of bending excitation in the donor and acceptor subunits, which is a result of interchange of donor and acceptor roles. The rotational distributions associated with the major channel, in which one water fragment has one quantum of bend, and the minor channel with both water fragments in the ground vibrational state are calculated and are in agreement with experiment.



## INTRODUCTION

The complex properties of water, which are due in large part to its hydrogen bond (H bond) network, have fascinated and challenged chemists since the early 1920s.<sup>1–6</sup> In the gas phase, experimental emphasis has been placed on investigations of clusters in the cold environment of molecular beams, with most reports focusing on spectroscopy.<sup>6,7</sup> The mechanism of vibrational predissociation (VP) of H-bonded clusters are at present much less understood.<sup>8</sup> As the smallest cluster, the water dimer serves as a benchmark for both experiment and theory.<sup>9,10</sup> Studies of H bond breaking in the dimer provide critical information on bond strength and energy relaxation, both of which are important in understanding these processes in complex water networks, such as clusters, liquids, solids, water chains, and other unusual structures.<sup>6,7,11–14</sup>

The atmospheric importance of the water dimer continues to be the subject of intense interest.<sup>15–18</sup> In this context, an accurate value of the bond dissociation energy ( $D_0$ ) of the dimer is crucial in assessing the contributions of the water dimer to absorption in the atmosphere.<sup>15</sup> Pairwise interactions are also important in amorphous solid water, which is the most common form of water in the universe.<sup>13</sup> It is therefore quite surprising that so little is known about the VP dynamics of the water dimer.

Here, we report studies of VP following excitation of the H-bonded OH and OD stretch of  $(H_2O)_2$  and  $(D_2O)_2$ , respectively, and determine  $D_0$  and correlated internal states

of monomer fragments. Upon excitation of the dimer, two channels are energetically open for  $(H_2O)_2$  and  $(D_2O)_2$ : (1)  $(000) + (000)$  and (2)  $(000) + (010)$ , where  $(000)$  and  $(010)$  are the ground and first bending vibrational states of the fragment, respectively (relevant energies are listed in Table S1 of Supporting Information (SI)).

Experimental studies of state-specific energy transfer and H-bond-breaking pathways of water-containing dimers are scarce because of difficulties in detecting water fragments. It is only recently that water fragments were detected state-selectively in VP of dimers,<sup>19,20</sup> and the  $D_0$  of  $(H_2O)_2$  was reported with spectroscopic accuracy ( $1105 \pm 10 \text{ cm}^{-1}$ )<sup>20</sup> in excellent agreement with theory ( $1103 \pm 5 \text{ cm}^{-1}$  [ref 21] and  $1108.2 \text{ cm}^{-1}$  [ref 10]). In this contribution, we report for the first time the experimental determination of  $D_0$  for  $(D_2O)_2$ . We also determine pair-correlated fragment state distributions (i.e., the cofragment state distribution correlated with a specific rovibrational state of the other monomer fragment) for  $(H_2O)_2$  and  $(D_2O)_2$ . Such pair-correlated distributions can provide rigorous tests of mechanisms.

Recently, Czakó et al.<sup>9</sup> calculated  $D_0 = 1244 \pm 5 \text{ cm}^{-1}$  for  $(D_2O)_2$  and reported preliminary quasi-classical trajectory (QCT) calculations predicting that the predominant channel in the VP of  $(H_2O)_2$  and  $(D_2O)_2$  was  $(000) + (010)$ . The

Received: June 6, 2012

Published: August 23, 2012



theoretical calculations provide complementary information, which is partly inaccessible in experiments. For example, the calculations show that bending vibrational excitation is distributed equally between fragments corresponding to the donor (*d*) and acceptor (*a*) units. The new QCT calculations reported here provide for the first time fragment rotational distributions correlated separately with channels (1) and (2). This information is currently impossible to obtain experimentally. In addition, we analyze representative trajectories and report vector correlations in fragment rotations. The combined theoretical and experimental results reveal new insights about energy transfer and the VP mechanism.

## ■ EXPERIMENTAL METHODS

Two experimental methods of data collection were used: (i) time-of-flight mass spectrometry combined with 2 + 1 resonance-enhanced multiphoton ionization (REMPI) for spectroscopic investigations of water monomer fragments, and (ii) velocity map imaging (VMI) for deriving internal energy distributions of cofragments (nondetected fragments) as well as determining  $D_0$  of  $(\text{H}_2\text{O})_2$  and  $(\text{D}_2\text{O})_2$ .

The experimental procedures are similar to those used in the previous studies.<sup>19,20,22,23</sup> The dimers were formed in a pulsed supersonic molecular beam by expanding ~2% water in helium at a stagnation pressure of ~2 atm through the 0.5 mm orifice of a pulsed valve. Focused infrared (IR) radiation excited the H-bonded OH and OD stretch of  $(\text{H}_2\text{O})_2$  and  $(\text{D}_2\text{O})_2$  at 3602 and  $2634 \text{ cm}^{-1}$ , respectively. Tightly focused ultraviolet (UV) radiation ionized state-selected  $\text{H}_2\text{O}$  and  $\text{D}_2\text{O}$  fragments, scanning through the  $\tilde{\text{C}}^1\text{B}_1(000) \leftarrow \tilde{\text{X}}^1\text{A}_1(000 \text{ and } 010)$  bands using REMPI. The  $\tilde{\text{C}}^1\text{B}_1$  excited state of  $\text{H}_2\text{O}$  has a short lifetime due to predissociation, particularly for high  $J''$  with high  $K_a'$  levels,<sup>24</sup> which prevents us from detecting certain high rotational levels and makes the detection scheme more dependent on excitation conditions. For this reason, the  $\text{H}_2\text{O}$  REMPI spectra are also noisier compared to those of  $\text{D}_2\text{O}$ , which is less predissociative.<sup>24</sup> On the other hand, the  $\text{D}_2\text{O}$  spectra are more congested due to smaller spacings between rotational levels.

Spectra were collected by alternating “IR on” and “IR off” conditions. IR laser conditions (timing, focusing, power) were optimized to ensure single-photon absorption. UV laser conditions were optimized for the best signal-to-noise ratio. Expansion conditions (water concentration, helium backing pressure) were optimized to maximize signal from the dimer. A cryopumping system cooled by liquid nitrogen was installed to reduce background water during data acquisition. The dimer H-bonded OH and OD stretch is red-shifted by  $\sim 150 \text{ cm}^{-1}$  from the monomer antisymmetric stretch, the trimer H-bonded stretch is  $40\text{--}70 \text{ cm}^{-1}$  red-shifted from the dimer, and higher clusters are further red-shifted from the trimer.<sup>25,26</sup> The combination of IR laser and expansion conditions allows excitation of water dimer without contributions from higher clusters. The combination of UV laser conditions and cryopumping maximizes detection of the water fragment upon dimer dissociation and minimizes background signals from water monomers. The VMI arrangement and data analysis methods have been described before.<sup>19,23</sup> Two-dimensional projections of the velocity distributions were collected using event counting and reconstructed to give velocity or speed distributions using the BASEX method.<sup>27</sup>

## ■ COMPUTATIONAL METHODS

The QCT calculations were performed with the ab initio HBB2 PES.<sup>21</sup> Standard normal-mode sampling was applied to prepare the initial quasi-classical states by giving harmonic zero-point energy (ZPE) to each mode and an extra quantum of excitation to the H-bonded OH and OD stretch fundamental, i.e., almost a local mode of the donor. The total rotational angular momentum of the dimers was set to zero. A total of 30,000 trajectories for each dimer were propagated for about 25 ps using a 0.25 fs time step. For  $(\text{D}_2\text{O})_2$  we ran 10,000 longer (50 ps) trajectories as well. The product states of the fragments were analyzed for dissociated trajectories with O–O distance  $> 10 \text{ \AA}$ . At 25

ps about 84% of the  $(\text{H}_2\text{O})_2$  trajectories dissociated, but only 25% of the  $(\text{D}_2\text{O})_2$  trajectories did. This latter value increases to about 64% at 50 ps.

We determined the normal mode quantum numbers for the water fragment pairs using the procedure described previously.<sup>9,28</sup> The rovibrational distributions were computed by the efficient Gaussian binning procedure (1GB).<sup>9,28</sup> In the present implementation, 1GB means one Gaussian weight for each fragment based on its total vibrational energy; thus, the weight of a correlated state is the product of two Gaussians. 1GB assigns small weights for trajectories in which either fragment violates ZPE, thereby effectively addressing the well-known ZPE issue of the QCT method. (Note that the Gaussians have finite widths; in the present case the full width at half-maximum is 0.1, which corresponds to about 900 and 700  $\text{cm}^{-1}$  for  $\text{H}_2\text{O}$  and  $\text{D}_2\text{O}$ , respectively. Thus, 1GB can allow small nonzero weights for energetically closed states.)

## ■ RESULTS AND DISCUSSION

IR action spectra of the excited dimers were obtained by monitoring  $\text{H}_2\text{O}$  and  $\text{D}_2\text{O}$  fragments in selected rovibrational states by REMPI while scanning the IR laser frequency (see Figure S1 in SI). The positions and shapes of the H-bonded OH and OD stretch bands, which indicate that the absorbed species are dimers, were similar to previously reported spectra.<sup>25,29</sup> The lifetimes of excited  $(\text{H}_2\text{O})_2$  and  $(\text{D}_2\text{O})_2$  are 80 ps and 5 ns, respectively.<sup>25</sup>

Figure 1 shows REMPI spectra of  $\text{H}_2\text{O}$  and  $\text{D}_2\text{O}$  fragments in the  $\tilde{\text{C}}^1\text{B}_1(000) \leftarrow \tilde{\text{X}}^1\text{A}_1(000 \text{ and } 010)$  bands. Spectral congestion and/or upper state predissociation prevent us from converting the REMPI spectra into complete rotational populations of the fragments. However, the spectra in a, b, and d of Figure 1 were simulated fairly well with rotational temperatures of  $250 \pm 50$ ,  $250 \pm 50$ , and  $150 \pm 50 \text{ K}$ , respectively. No temperature gave a good fit to the spectrum in Figure 1c; specifically, several prominent peaks include unusually large contributions from  $J'' > 11$  (see below).

Several isolated rotational transitions of  $\text{H}_2\text{O}$  (000) and (010) fragments were used for imaging, as described before.<sup>20</sup> The REMPI spectrum of fragment  $\text{D}_2\text{O}$  (000), with allowed transitions from  $J'' = 0$  to 16 (Figure 1c), is very congested, and we could find no unblended lines suitable for accurate determination of  $D_0$ . Fortunately, the  $\tilde{\text{C}}^1\text{B}_1(000) \leftarrow \tilde{\text{X}}^1\text{A}_1(010)$  band has only few ( $J'' \leq 5$ ) energetically allowed transitions, and images from isolated transitions of  $\text{D}_2\text{O}$  (010) fragments were used for determination of  $D_0$ .

Figure 2 shows representative velocity distributions obtained by VMI. The recorded two-dimensional projections of ionized fragments were reconstructed to three-dimensional images.<sup>19,20,22,23</sup> Reconstructed images in velocity space were obtained by summing over the isotropic angular distribution for each radius. The isotropy of the angular distributions reflects the slowness of the dissociation processes. The velocity distributions were used to determine the rotational populations of  $\text{H}_2\text{O}$  and  $\text{D}_2\text{O}$  cofragments pair-correlated with each monitored rovibrational state, as described before.<sup>19,20,22,23</sup>

Fitting was accomplished by assigning a Gaussian-shaped curve to rotational levels<sup>31,32</sup> of each cofragment vibrational state. The positions of these Gaussians were determined by conservation of energy,

$$\begin{aligned} E_{\text{rot}}(\text{dimer}) + h\nu = D_0 + E_{\text{T}} + E_{\text{vib,rot}}(\text{mon}) \\ + E_{\text{vib,rot}}(\text{cofrag}) \end{aligned}$$

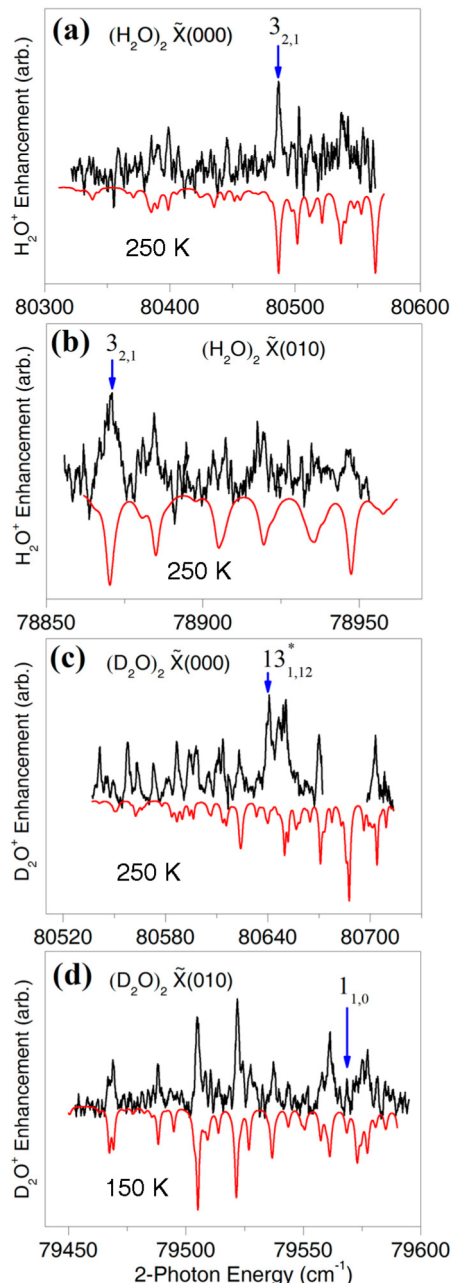


**Figure 1.** Fragment yield spectra of  $(\text{H}_2\text{O})_2$  and  $(\text{D}_2\text{O})_2$ . The black curves correspond to the fragments  $2 + 1$  REMPI enhancement spectra scanning the (a)  $\text{H}_2\text{O} \tilde{\text{C}}^1\text{B}_1(000) \leftarrow \tilde{\text{X}}^1\text{A}_1(000)$  band; (b)  $\text{H}_2\text{O} \tilde{\text{C}}^1\text{B}_1(000) \leftarrow \tilde{\text{X}}^1\text{A}_1(010)$  band; (c)  $\text{D}_2\text{O} \tilde{\text{C}}^1\text{B}_1(000) \leftarrow \tilde{\text{X}}^1\text{A}_1(000)$  band; and (d)  $\text{D}_2\text{O} \tilde{\text{C}}^1\text{B}_1(000) \leftarrow \tilde{\text{X}}^1\text{A}_1(010)$  band. The red curves correspond to PGOPHER simulations<sup>30</sup> with known spectroscopic parameters,<sup>24</sup> and using the labeled rotational temperatures. Assigned REMPI transitions selected for images are labeled. \* denotes a blended transition with a major contribution from  $J''_{\text{KaKc}} = 13_{1,12}$ .

where  $E_{\text{rot}}(\text{dimer})$  is the dimer rotational energy estimated from IR spectra ( $5$  and  $7 \pm 5 \text{ cm}^{-1}$  for  $(\text{H}_2\text{O})_2$  and  $(\text{D}_2\text{O})_2$ , respectively);  $h\nu$  is the IR photon energy;  $E_{\text{T}}$  is the measured center-of-mass (c.m.) translational energy ( $\alpha$  velocity<sup>2</sup>); and  $E_{\text{vib,rot}}(\text{mon})$  (defined by REMPI) and  $E_{\text{vib,rot}}(\text{cofrag})$  are the rovibrational energies of the monitored fragment and the cofragment, respectively. The positions of the Gaussians were shifted together by adjusting  $D_0$  until both the observed

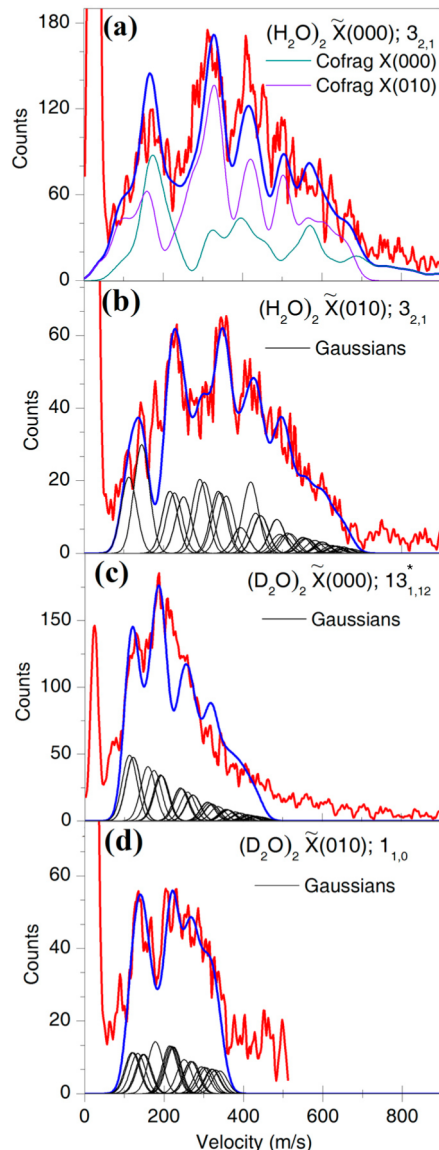


**Figure 2.** Velocity distributions from reconstructed images obtained by monitoring state-selected fragments. The red curves show experimental results of state-selected  $\text{H}_2\text{O}$  or  $\text{D}_2\text{O}$  fragments, and the blue ones correspond to total integrated simulations. The Gaussians (black curves) in (b), (c), and (d) are the energetically allowed rotational levels of the cofragment. In (a) the Gaussians were integrated to obtain the green and purple curves for cofragments in the (000) and (010) state, respectively. A ratio of (000):(010) = 1:2 was used.

structure and the maximum velocity were well matched in all the images. The widths of the Gaussians (44 and 39 m/s for  $\text{H}_2\text{O}$  and  $\text{D}_2\text{O}$  fragments, respectively) were obtained from previous calibration experiments.<sup>19</sup>

In all cases reasonable fits to the velocity distributions were obtained by using an exponentially decaying function for the heights of the Gaussians, corresponding to decrease in rotational population with increasing  $E_{\text{T}}$ . However, to obtain best fits, state-to-state population fluctuations have to be included. For images in the (000) state, because of the overlap of two sets of rotational levels in the cofragment [cofragments in (000) and (010) states] and congestion of the  $J''_{\text{KaKc}}$  levels, it was impossible to adjust the height of each Gaussian unambiguously for a detailed rotational population distribution.

For images in the (010) state, where the cofragment is only allowed in the (000) state, the heights of the Gaussian curves were adjusted to obtain the best fit. As before,<sup>19,20,22,23</sup> we find that the  $D_0$  value derived from fitting multiple images is narrowly constrained by the fits to unique structures in each image, which are determined by rotational level positions. The same  $D_0$  value is obtained whether we use smooth population functions or adjust the height of each Gaussian to obtain the best fit to the overall velocity distribution.

Figure 2a shows a velocity distribution obtained by monitoring  $\text{H}_2\text{O}$  (000)  $J''_{\text{KaKc}} = 3_{2,1}$ , where the cofragments are formed in both the (000) and (010) states. Best fits are obtained with a ratio of (000):(010) = 1:2 in the cofragments (see Figure S3 in SI for additional images). Figure 2b shows the image obtained by monitoring  $J''_{\text{KaKc}} = 3_{2,1}$  of (010).

When monitoring rotational levels in  $\text{D}_2\text{O}$  (000) up to  $J'' = 5$ , both the (000) and (010) vibrational levels of the cofragment can be populated, but only the (000) level is allowed for  $J'' > 5$ . As described above, all spectral lines of  $\text{D}_2\text{O}$  (000) are blended; thus, the exact ratio of (000):(010) in the cofragments cannot be determined from the images, but the fits show that a large fraction of the fragments are in the (010) state. Indeed, a REMPI spectrum of  $\text{D}_2\text{O}$  (010) fragments was obtained (Figure 1d), and  $D_0$  of  $(\text{D}_2\text{O})_2$  was determined by fitting four images of isolated transitions of  $\text{D}_2\text{O}$  (010). Figure 2d shows a representative velocity distribution, and others are shown in SI (Figure S4). After internal energy and error corrections, these images give  $D_0 = 1244 \pm 10 \text{ cm}^{-1}$ , in excellent agreement with theory.<sup>9</sup> Images obtained by monitoring blended transitions of  $\text{D}_2\text{O}$  (000) are consistent with this value (Figures 2c and S5 [SI]).

Fitting the unique structures in the images puts the uncertainty of the fits at 2–8  $\text{cm}^{-1}$ , depending on the signal-to-noise ratio in each image. The uncertainty in internal energy of the dimer is estimated to be  $\pm 5 \text{ cm}^{-1}$ , and IR frequency calibration adds another 1  $\text{cm}^{-1}$  to the uncertainty. Taking the weighted average of all our data and combining random and systematic uncertainties, we arrive at the uncertainty quoted above.

The  $\text{D}_2\text{O}$  (000) images confirm that the intense peaks in the REMPI spectrum that could not be fit by a 250 K rotational temperature include large contributions from high  $J''$ 's. For example, in Figure 2c, the high  $J''$  state gives rise to the prominent low-velocity features, and additional images with major contributions from  $J'' = 12$  and 13 are shown in Figure S5 (SI). Our inability to observe a comparable excess population in high  $J''$  levels of  $\text{H}_2\text{O}$  (000) may be due to the faster predissociation of the  $\tilde{\text{C}}^1\text{B}_1$  state of  $\text{H}_2\text{O}$ .<sup>24</sup>

The experimental results give rotational distributions of the cofragments pair-correlated with specific  $\text{H}_2\text{O}$  and  $\text{D}_2\text{O}$  rovibrational levels, and these distributions encompass all the rotational states allowed by energy conservation. In spite of some fluctuations in state populations, they show consistent preferential population of high rotational levels that minimize translational energy release. The trajectory calculations, on the other hand, give the overall rotational distributions for each product vibrational channel, as described below.

Calculated channel-specific rotational distributions for  $(\text{D}_2\text{O})_2$  are shown in Figure 3. The rotational distributions for the (000) + (010) channel are significantly colder than those for the (000) + (000) channel, as expected from the reduced available energy. The distributions are broad, each peaking at  $J''$  around of 4 and 7, respectively. (Note that for

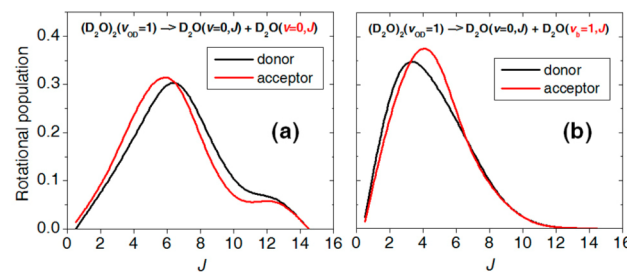


**Figure 3.** Calculated vibrational state-specific rotational distributions of  $\text{D}_2\text{O}$  fragments from VP of  $(\text{D}_2\text{O})_2$ . (a) Ground vibrational state products; (b) one bend-excited monomer fragment.

(000) + (010) the maximum allowed  $J''$  is 5, but nonzero computed populations for  $J'' > 5$  are possible, owing to the highly asymmetric top nature of the monomers and the finite widths (about  $700 \text{ cm}^{-1}$  for  $\text{D}_2\text{O}$ ) of the Gaussians allowing a few hundred  $\text{cm}^{-1}$  ZPE violation, which is small relative to the ZPE of the monomers, but not small enough to force the threshold in the rotational distributions.) The rotational distributions corresponding to the donor and acceptor fragments in each channel are similar, and there is an equal likelihood that the bending excitation resides in the donor or acceptor fragments.<sup>9</sup> This indicates that energy is shared between the two monomers, even though the OD stretch excitation has been placed initially in the donor. The rotational distributions of the corresponding product channels in  $(\text{H}_2\text{O})_2$  are similar to those from  $(\text{D}_2\text{O})_2$  (see Figure S6 in SI). The average rotational energy in each  $\text{D}_2\text{O}$  fragment for the major (000) + (010) channel is  $75 \pm 20 \text{ cm}^{-1}$ .<sup>33</sup> This value is in good agreement with the experimental estimate of  $100 \pm 40 \text{ cm}^{-1}$ , obtained from the temperature simulation of the REMPI spectrum (Figure 1d).

We also examined vector correlations of the relative c.m. velocity vector ( $\mathbf{v}$ ) and the classical total angular momentum vector ( $\mathbf{J}$ ) integrated over the fragment states. The computed results show that  $\mathbf{v}$  and  $\mathbf{J}$  of either the donor or the acceptor fragment are correlated, since the scalar product of  $\mathbf{v}$  and  $\mathbf{J}$  shows a Gaussian-like distribution peaking at 0 (Figure 4). This indicates that both the donor and acceptor fragments are

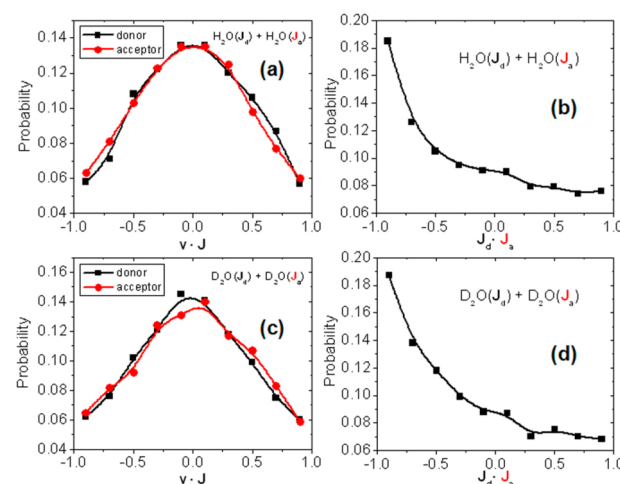


**Figure 4.** Correlation between the relative center of mass velocity vector ( $\mathbf{v}$ ) and the total angular momentum vector ( $\mathbf{J}$ ) of either the donor ( $\mathbf{J}_d$ ) or the acceptor ( $\mathbf{J}_a$ ) fragment [(a) and (c)] as well as correlation between the  $\mathbf{J}_d$  and  $\mathbf{J}_a$  vectors [(b) and (d)].

preferentially formed in rotational states with  $J$  vectors perpendicular, on average, to the relative velocity vector of the fragments. The  $J$  vectors of the two fragments are also correlated, favoring an antiparallel orientation that facilitates angular momentum conservation.

More insight into the dissociation dynamics is obtained by examining the time evolution of trajectories that lead to dissociation, and a  $(\text{H}_2\text{O})_2$  and a  $(\text{D}_2\text{O})_2$  trajectory can be seen as animations. A  $(\text{D}_2\text{O})_2$  trajectory animation terminating in  $(000) + (000)$  with a highly rotationally excited  $\text{D}_2\text{O}$  fragment is shown as animation 1). In addition, snapshots of a representative  $(\text{H}_2\text{O})_2$  trajectory are shown in Figure 5

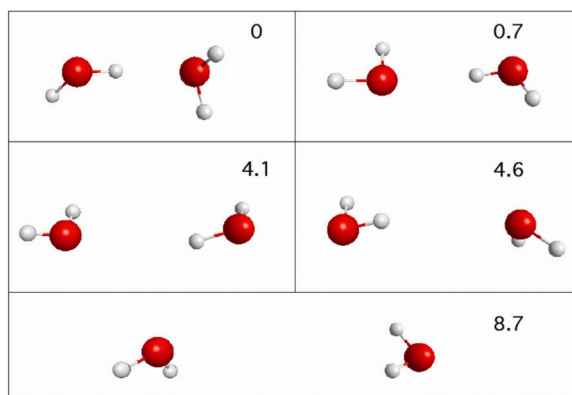


**Figure 5.** Selected frames labeled in picoseconds in increasing time sequence of a  $(\text{H}_2\text{O})_2$  trajectory leading to dissociation. Note the exchange of donor and acceptor (in the first picosecond) that occurs several times during the trajectory before dissociation occurs. Animation is available as animation 2.

(see also animation 2). As seen, the identity of the donor and acceptor switches; at later times and larger O–O distance, the two monomers assume a quasi-planar geometry; and finally we see dissociated monomers. Exchanges of donor and acceptor occur several times during the trajectory, which explains the similar rotational distributions as noted above. This facile exchange is a consequence of the low barriers (the largest being roughly  $620 \text{ cm}^{-1}$ ) for isomerization of the water dimer to the eight equivalent minima,<sup>34</sup> which are accurately reproduced by the PES.

The experimental and theoretical results described herein depict, for the first time, a detailed picture of the VP of the water dimer. Following excitation of the bonded OH and OD stretch of the donor, calculations show that vibrational energy is shared among the donor and acceptor vibrational levels. The major dissociation channel is  $(000) + (010)$  with equal probability of bending excitation in the donor and acceptor fragments, and the donor and acceptor have similar and broad rotational state distributions. The experimental pair-correlated distributions are also broad, with a nonstatistical rotational energy distribution in the cofragment biased in favor of high rotational levels that minimize translational energy release. There is also a clear preference for producing one fragment in the  $(010)$  state, in accordance with the momentum-gap law of energy transfer.<sup>35</sup>

The initial energy transfer out of the OH and OD stretch could involve coupling to two quanta of intramolecular bend and one or more intermolecular vibrations, since there are near-resonant pathways for both  $(\text{D}_2\text{O})_2$  and  $(\text{H}_2\text{O})_2$ . For example, in  $(\text{H}_2\text{O})_2$  the bound OH stretch ( $3601 \text{ cm}^{-1}$ ) is nearly

resonant with two quanta of intramolecular bend plus an intermolecular bend (see Table S2 in SI and ref 21).<sup>36</sup> Of course this energy transfer must then decay to one involving excitation of the dissociative degree of freedom, which often leaves one quantum of bend excitation in a fragment. One can envision scenarios where the initial bending excitation resides in one water molecule or is shared between the two water molecules (i.e., formation of  $(020)$  or  $(010) + (010)$ ).

As seen from the trajectories, the coupling of at least one bending quantum to the intermolecular modes involves extensive intramolecular vibrational redistribution among the intermolecular modes, including the exchange of donor and acceptor, which explains their final broad and similar rotational state distributions. The coupling to the dissociation coordinate is apparently inefficient, as both experiment and theory show dimer lifetimes  $>10 \text{ ps}$ .<sup>9,25</sup> However, while there is ample time for the energy to redistribute among the available vibrational states, only restricted paths lead eventually to dissociation. The result is that, while the rotational energy distributions are broad, they are not statistical. In fact, the propensity to generate one water fragment in the  $(010)$  state as well as in high rotational levels indicates that the momentum gap law, which predicts a preference for final fragment states that minimize translational energy release, is still manifest despite the extensive intramolecular vibrational redistribution and long dissociation time.

An intriguing aspect in the REMPI spectrum of  $\text{D}_2\text{O}$  (000) is the enhanced population of high rotational levels whose energies lie within  $100 \text{ cm}^{-1}$  of the  $1178 \text{ cm}^{-1} J''_{\text{KaKc}} = 0_{0,0}$  level of  $\text{D}_2\text{O}$  (010). The minor  $(000) + (000)$  channel may result in part from processes in which the excited dimer samples the repulsive part of the PES in an impulsive interaction, converting all the vibrational excitation into fragment rotation and translation,<sup>37</sup> thereby accessing high rotational levels. This, however, is a minor channel.

## CONCLUSION

The theoretical calculations of  $D_0$  of  $(\text{H}_2\text{O})_2$  and  $(\text{D}_2\text{O})_2$  are in excellent agreement with experiment, demonstrating the high quality of the water dimer PES. Trajectory calculations and experimental results both show broad rotational distributions of the monomer products. Theory and experiment both find the major channel to be  $(000) + (010)$ , indicating that the vibrationally excited H-bonded OH stretch relaxes via a pathway that preferentially leads to bend excitation in the monomer. Dissociation is slow and involves extensive intramolecular vibrational energy distribution in the dimer, but product state distributions are not statistical. In the future, we hope to extend these results to the cyclic water trimer—the smallest network of hydrogen bonds.

## ASSOCIATED CONTENT

### S Supporting Information

IR and REMPI spectra; additional images and rotational distributions; vibrational energies of the monomers and dimers. This material is available free of charge via the Internet at <http://pubs.acs.org>.

### W Web-Enhanced Features

Animations of trajectories of water dimer dissociation dynamics generated by QCT calculations are available in the HTML version of the paper.

## AUTHOR INFORMATION

### Corresponding Author

reisler@usc.edu (H.R.); jmbowma@emory.edu (J.M.B.)

### Present Address

<sup>§</sup>Laboratory of Molecular Structure and Dynamics, Institute of Chemistry, Eötvös University, P.O. Box 32, H-1518 Budapest 112, Hungary

### Notes

The authors declare no competing financial interest.

## ACKNOWLEDGMENTS

We thank Dr. Blithe E. Rocher and Dr. Andrew K. Mollner for helpful discussions. This work was supported by the U.S National Science Foundation Grants CHE-0951976 (H.R.) and CHE-1145227 (J.M.B.), and the Scientific Research Fund of Hungary Grant NK83583 (G.C.).

## REFERENCES

- (1) Latimer, W. M.; Rodebush, W. H. *J. Am. Chem. Soc.* **1920**, *42*, 1419–1433.
- (2) Pauling, L. *Proc. Natl. Acad. Sci. U.S.A.* **1928**, *14*, 359–362.
- (3) Bernal, J. D.; Fowler, R. H. *J. Chem. Phys.* **1933**, *1*, 515–548.
- (4) Pauling, L. *The Nature of the Chemical Bond and the Structure of Molecules and Crystals: An Introduction to Modern Structural Chemistry*; Cornell University Press: New York, 1939.
- (5) Scheiner, S. *Hydrogen Bonding: A Theoretical Perspective*; Oxford University Press: New York, 1997.
- (6) Keutsch, F. N.; Saykally, R. J. *Proc. Natl. Acad. Sci. U.S.A.* **2001**, *98*, 10533–10540.
- (7) Keutsch, F. N.; Cruzan, J. D.; Saykally, R. J. *Chem. Rev.* **2003**, *103*, 2533–2578.
- (8) Oudejans, L.; Miller, R. *Annu. Rev. Phys. Chem.* **2001**, *52*, 607–637.
- (9) Czakó, G.; Wang, Y.; Bowman, J. M. *J. Chem. Phys.* **2011**, *135*, 151102.
- (10) Leforestier, C.; Szalewicz, K.; van der Avoird, A. *J. Chem. Phys.* **2012**, *137*, 014305.
- (11) Rey, R.; Möller, K. B.; Hynes, J. T. *Chem. Rev.* **2004**, *104*, 1915–1928.
- (12) Bakker, H. J.; Skinner, J. L. *Chem. Rev.* **2010**, *110*, 1498–1517.
- (13) Smith, R. S.; Petrik, N. G.; Kimmel, G. A.; Kay, B. D. *Acc. Chem. Res.* **2011**, *45*, 33–42.
- (14) Paesani, F.; Xantheas, S. S.; Voth, G. A. *J. Phys. Chem. B* **2009**, *113*, 13118–13130.
- (15) Vaida, V. *J. Chem. Phys.* **2011**, *135*, 020901.
- (16) Scribano, Y.; Goldman, N.; Saykally, R. J.; Leforestier, C. *J. Phys. Chem. A* **2006**, *110*, 5411–5419.
- (17) Goldman, N.; Leforestier, C.; Saykally, R. J. *J. Phys. Chem. A* **2004**, *108*, 787–794.
- (18) Goldman, N.; Fellers, R. S.; Leforestier, C.; Saykally, R. J. *J. Phys. Chem. A* **2000**, *105*, 515–519.
- (19) Rocher-Casterline, B. E.; Mollner, A. K.; Ch'ng, L. C.; Reisler, H. *J. Phys. Chem. A* **2011**, *115*, 6903–6909.
- (20) Rocher-Casterline, B. E.; Ch'ng, L. C.; Mollner, A. K.; Reisler, H. *J. Chem. Phys.* **2011**, *134*, 211101.
- (21) Shank, A.; Wang, Y.; Kaledin, A.; Braams, B. J.; Bowman, J. M. *J. Chem. Phys.* **2009**, *130*, 144314.
- (22) Casterline, B. E.; Mollner, A. K.; Ch'ng, L. C.; Reisler, H. *J. Phys. Chem. A* **2010**, *114*, 9774–9781.
- (23) Mollner, A. K.; Casterline, B. E.; Ch'ng, L. C.; Reisler, H. *J. Phys. Chem. A* **2009**, *113*, 10174–10183.
- (24) Yang, C.-H.; Sarma, G.; ter Meulen, J. J.; Parker, D. H.; Western, C. M. *Phys. Chem. Chem. Phys.* **2010**, *12*, 13983–13991.
- (25) Paul, J. B.; Provencal, R. A.; Chapo, C.; Petterson, A.; Saykally, R. J. *J. Chem. Phys.* **1998**, *109*, 10201–10206.
- (26) Paul, J. B.; Collier, C. P.; Saykally, R. J.; Scherer, J. J.; O'Keefe, A. *J. Phys. Chem. A* **1997**, *101*, 5211–5214.
- (27) Dribinski, V.; Ossadchi, A.; Mandelshtam, V. A.; Reisler, H. *Rev. Sci. Instrum.* **2002**, *73*, 2634–2642.
- (28) Czakó, G.; Bowman, J. M. *J. Chem. Phys.* **2009**, *131*, 244302.
- (29) Huang, Z. S.; Miller, R. E. *J. Chem. Phys.* **1989**, *91*, 6613–6631.
- (30) Western, C. M. *PGOPHER*, a Program for Simulating Rotational Structure; University of Bristol: Bristol, U.K., 2009; <http://pgopher.chm.bris.ac.uk>.
- (31) Tennyson, J.; Zobov, N. F.; Williamson, R.; Polyansky, O. L.; Bernath, P. F. *J. Phys. Chem. Ref. Data* **2001**, *30*, 735–831.
- (32) Mellau, G.; Mikhailenko, S. N.; Starikova, E. N.; Tashkun, S. A.; Over, H.; Tyuterev, V. G. *J. Mol. Spectrosc.* **2004**, *224*, 32–60.
- (33) The average rotational energy of  $75 \text{ cm}^{-1}$  was obtained by using 1GB and giving zero weights to trajectories in which the sum of the rotational energies of the fragments is larger than the maximum available rotational energy of  $210 \text{ cm}^{-1}$ . Without this rotational energy constraint, 1GB provides an average rotational energy of  $180 \pm 20 \text{ cm}^{-1}$ . Note that the error bars correspond to statistical uncertainties (without considering systematic uncertainties).
- (34) Tschumper, G. S.; Leininger, M. L.; Hoffman, B. C.; Valeev, E. F.; Schaefer, H. F., III; Quack, M. *J. Chem. Phys.* **2002**, *116*, 690–701.
- (35) Ewing, G. E. *J. Phys. Chem.* **1987**, *91*, 4662–4671.
- (36) Note that the vibrational levels are measured or calculated for ground state dimer and not for a dimer with one quantum of OH and OD stretch. Because most of the values are taken from matrix isolation data, they differ slightly from gas phase values. Also, the floppiness of the dimer may give values that deviate from the average equilibrium values.
- (37) Pritchard, M.; Parr, J.; Li, G.; Reisler, H.; McCaffery, A. *J. Phys. Chem. Chem. Phys.* **2007**, *9*, 6241–6252.